PROCEEDINGS, 51st Workshop on Geothermal Reservoir Engineering
Stanford University, Stanford, California, February 9-11, 2026
SGP-TR-230

Simple Method to Extract Heat Transfer Area and Predict Thermal Lifetime

Adam J. Hawkins

School of Civil and Environmental Engineering and Earth Sciences, Clemson University, Clemson, SC

ahawki9@clemson.edu

Keywords: heat transfer area, tracer, pressure drop, thermal performance, short circuit, premature thermal breakthrough, predictive models

ABSTRACT

It is a well-established concern that uncertainty in effective interwell heat transfer areas introduce significant financial risk. This is true, because heat transfer area and mass flow rates determine transient production well temperatures. Here, a simple method to predict thermal performance that already exists in peer-reviewed literature is presented in a pedagogical fashion. The method utilizes joint pressure-tracer calibration to determine effective heat transfer area. Using a suitable analytical model for heat transfer, one can then readily predict thermal performance. Several case studies are presented, including uncertainty analysis. The results emphasize the necessity of performing both tracer tests and pressure analysis.

1. INTRODUCTION

From microfluidics to planetary science, hydrodynamic lubrication theory predicts the frictional loss of Newtonian fluids due to viscous forces (i.e., "Poiseuille flows"). Even in rough-walled conduits (e.g., Gloss and Herwig, 2010), this special case provides exact, closed form solutions to the Navier-Stokes equations where the pressure gradient ∇P (Pa), is related to mean fluid velocity, u (m/s), as

$$u = \frac{k}{\mu} \nabla P \tag{1}$$

where k is permeability (m^2) and μ is dynamic fluid viscosity (Pa.s). A problem of particular importance arises when a body's surface area can vary independently of its volume (e.g., microfluidics, fractured rock hydrology, volcanology, energy functional materials, and carbon sequestration). In these circumstances, estimating the body's volume does not enable independent calculation of surface area. In contrast, identifying the volume of a sphere or a cylindrical pipe does constrain surface area, because the two quantities are both proportional to radius r.

Here, fluid mechanics and kinematics are coupled, and a simple analytical model is discovered that will calculate the effective area available for "no-slip" fluid flow given measurement of characteristic time and frictional pressure drop. I first use dimensional analysis to show that volume and surface area can be constrained by knowledge of characteristic transit time and frictional pressure drop. Then I show that the interfacial surface area of an internal flow in a channel can be computed for a specified volumetric flow rate Q. Then, mesoscale experiments in a 10 x 10 m fractured-rock field laboratory serve as a test case for determining surface area given frictional pressure drop and characteristic time at temperatures of 10 to 74 °C and pressures of 10^3 to 10^5 Pa. The computed area is then evaluated against independent measures obtained from non-conservative tracer tests, numerical models, and geophysical imaging.

2. THEORETICAL DEVELOPMENT

In this section, dimensional analysis results in a diffusive master equation that relates frictional energy dissipation E_f (kg^{1}m^{2}s^{-2}) of fluid flow in a non-deformable geometry of arbitrary shape with a finite volume V_f (m^3) and 'no-slip' surface area A_s (m^2). The dimensionless Poiseuille number (Janasek et al., 2006) is then employed to describe arbitrary geometries. Three specific geometries are described, including circular pipes, spheres, and parallel plates.

Under creeping fluid flow conditions at low Reynolds numbers Re, the coefficient of friction N_f varies linearly in proportion to Re. These two dimensionless quantities are generally defined as $N_\mathrm{f} = F/(A\rho\bar{u}^2)$ and $Re = \bar{u}L/\nu$, where F is the frictional force under consideration (kg^{1}m^{1}s^{-2}), ρ is mass density (kg^{1}m^{-3}), $\bar{u}$ is mean speed (m/s), A is the representative area (m^2), and L is the length scale (m) corresponding to the macroscopic velocity gradient of interest.

The representative area is commonly defined as the cross-sectional area A_x for buoyancy-induced displacement of a solid sphere in a fluid medium (i.e., Stokes law). Under creeping fluid flow conditions, however, a more representative area is defined as the surface area of a three-dimensional 'no-slip' interface, as discussed on page 236 in the fluid dynamics textbook by G. K. Batchelor (Batchelor_2000). Similarly, a 'no-slip' surface area is generally assumed for other hydrodynamic formulations at low Reynolds number, including the Hele-Shaw equation for fully developed, laminar flow between parallel plates (Hawkins et al., 2020) and the Hagen-Poiseuille equation for circular pipes (Janasek et al., 2006).

To begin with, the friction factor and the Reynolds number are given definitions following the treatment of hydrodynamics at low Reynolds number described in Hawkins et al. (2020). The resulting definition of Re is

$$Re \equiv \frac{f}{\nu}\frac{V_f \Delta x}{A_s}, \tag{2}$$

where f (s^{-1}) is defined as the reciprocal of the characteristic transit time of the system, V_f is the fluid volume (m^3), Δx is a body's observable length (m) in the direction of transport (e.g., sphere diameter, pipe length, etc.), and A_s is the surface area (m^2) of the three-dimensional solid-fluid interface **(Fig. 1).**

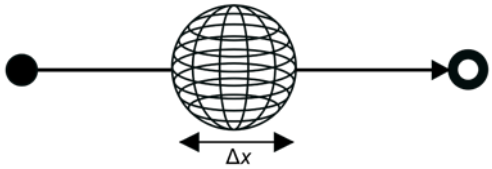

Figure 1: Schematic illustration of the geometric prototype. The variables shown on the figure are employed during the development of the diffusive master equation for a spherical body, where Δx is the body's length in the direction of transport.

The friction factor, N_f, is defined here as

$$N_f \equiv \frac{E_f}{mf^2}\left(\frac{V_f}{\Delta x^3 A_s}\right), \tag{3}$$

where E_f is the frictional energy loss (J) and m is the fluid mass displaced (kg) in an observed interval. Finally, the Poiseuille number is determined as the product of the friction factor and the Reynolds number. Rearranging the resulting expression yields the diffusive master equation and frictional power loss $\dot{E}_f$ (W) is given as

$$\dot{E}_f = N_{Po}\dot{m}\,\nu\left[\frac{A_s \Delta x}{V_f}\right]^2 f, \tag{4}$$

where $\dot{m}$ is the mass flow rate (kg/s) and the Poiseuille number N_{Po} is equal to three for parallel plates, two for circular pipes, and 1/3 for a sphere (see next section for further details) (Hawkins et al., 2022; Tester et al., 2021).

3. VALIDATION THROUGH CORRESPONDENCE WITH EXISTING MODELS

Eq. (4) suggests that surface area can be extracted from experiments if all other parameters are known. To demonstrate its validity, this section shows that the Hagen-Poiseuille equation (Lee et al., 2016; Oh et al., 2012; Secchi et al., 2016), Stokes law (e.g., Cassidy et al., 2018), and the Hele-Shaw equation (Zouache et al., 2016; Bahrami et al., 2006; Mutch et al., 2019; Stone et al., 2004) can be recovered if N_{Po} 2, $1/3$, or 3, respectively. Following this correspondence, I show how surface area can be extracted that corresponds physically to the effective area available for no-slip laminar fluid flow.

3.1 Hagen-Poiseuille Equation

The Hagen-Poiseuille equation describes mean fluid velocity across a parabolic profile in a cylindrical pipe (**Fig. 2**). It is derived from the Navier-Stokes equations with assumptions that include: (1) a no-slip condition exists at the solid-liquid interface; (2) the conduit walls are non-deformable; (3) the flowing fluid is incompressible and Newtonian; and (4) the maximum fluid velocity exists along the centerline of the cylindrical pipe. Here, I show that an identical derivation can be made directly from **Eq. (4)** if the following conditions are specified: (1) $N_{Po} = 2$; (2) $\Delta x = L$; (3) $V_f = \pi r^2 L$; and (4) $A_s = 2\pi r L$. With these specifications the Hagen-Poiseuille equation is recovered and $u = r^2/(8\mu) \times \Delta P/L$.

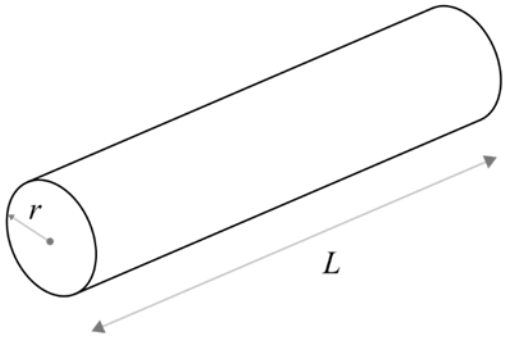

Figure 2: Circular pipe with fluid movement given by the Hagen-Poiseuille equation.

3.2 Stokes Law

Stokes law for buoyancy-driven flows can describe the ascent of a spherical body with radius r suspended within a fluid of contrasting density $\Delta\rho$ (**Fig. 3**). It is derived from the Navier-Stokes equations with assumptions similar to those listed above for the Hagen-Poiseuille equation, including: (1) a no-slip condition exists across the entire interfacial surface area of the sphere; (2) the size and shape of the sphere is uniform across Δx and τ; and (3) the displaced fluid surrounding the sphere is incompressible and Newtonian. As shown for the Hagen-Poiseuille equation, Stokes law is recovered directly from **Eq. (4)**. if: (1) $N_{\mathrm{Po}} = 1/3$; (2) $\Delta x = 2r$; (3) $V_{\mathrm{f}} = 4/3\,\pi r^3$; (4) $A_s = 4\pi r^2$; and (5) $\Delta P = \Delta\rho g \Delta x$, where g is the gravitational acceleration vector. With these specifications Stokes law is recovered and $u = \Delta\rho r^2 g/(3\mu)$.

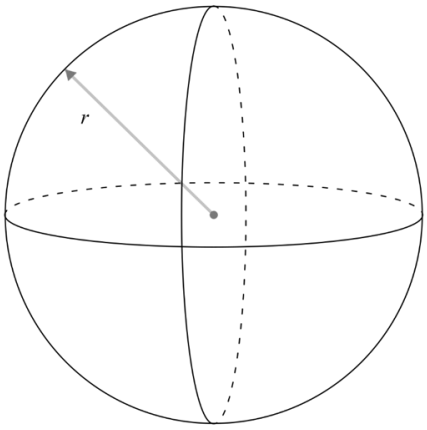

Figure 3: Spherical body with buoyancy-driven movement given by Stokes law.

3.3 Hele-Shaw Equation

As is the case for the Hagen-Poiseuille equation and Stokes law, the Hele-Shaw equation is conventionally derived directly from the Navier-Stokes equations (**Fig. 4**). Assumptions made in its derivation include: (1) a no-slip condition exists at the solid-liquid interfaces of the two parallel plates; (2) the width, W, of the plates perpendicular to the velocity vector is much greater than the aperture spacing, b, between the two plates; (3) both W and b are constant and uniform in space and time; (4) the flowing fluid is incompressible and Newtonian; and (5) the maximum fluid velocity exists uniformly along a plane located at the center of the aperture. If it is specified that: (1) $N_{\mathrm{Po}} = 3$; (2) $\Delta x = L$; (3) $V_{\mathrm{f}} = bWL$; and (4) $A_s = 2WL$, then the Hele-Shaw equation is recovered from equation (1) and $u = b^2/(12\mu) \times \Delta P/L$.

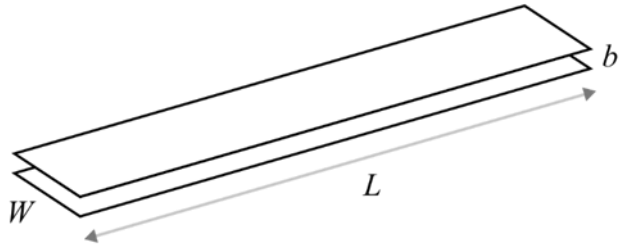

Figure 4: Parallel plate geometry with fluid flow described by the Hele-Shaw equation. Volume and surface area of the fluid-filled void are given as $V_{\mathrm{f}} = bWL$ and $A_s = 2WL$, respectively, where *b*, *W*, and *L* are the aperture, flow channel width, and flow channel length, respectively.

3.4 Effective Area Equation

As discussed in the introduction section, the interfacial surface area of a rectangular channel cannot be determined directly from a known volume, because the two quantities vary independently. Therefore, the surface area available for heat transfer or adsorption/absorption cannot be determined even if velocity and/or volume are known. In contrast to conventional models of a Hele-Shaw geometry, Eq. (4) suggests that if volumetric flow rate Q and characteristic time $\tau = f^{-1}$ are specified, then effective surface area can be determined. With $V_{\mathrm{f}} = Q\tau$ and a specified flow channel length L, the combined surface area of the upper and lower surfaces of a rectangular channel can be calculated as

$$A_s = \frac{V_{\mathrm{f}}}{L}\sqrt{\frac{\Delta P\tau}{3\mu}}. \tag{5}$$

4. MESOSCALE FIELD VALIDATION OF THE AREA LAW

To demonstrate how to employ **Eq. (5)** for calculating effective heat transfer area, mesoscale field experiments at the Altona Field Laboratory (AFL) (10 x 10 m well field) are utilized (**Fig. 5**). The field study targeted a naturally occurring, sub-horizontal bedding plane fracture located roughly 7.6 m below ground surface. The highly permeable target fracture is contained within the Potsdam sandstone. The very low matrix porosity of the Potsdam sandstone at the AFL (~1-3%) makes this formation an ideal analog to the crystalline rocks typical in geothermal reservoirs, for example. Since development of the field site began in 2004, field tests at the site have included geophysical imaging via Ground Penetrating Radar (GPR), periodic hydraulic tests, and testing of carbon-cored nanoparticle tracers and reactive tracers (e.g., Hawkins et al., 2017a; Hawkins et al., 2017b; Hawkins et al., 2018; Guiltinan and Becker, 2015; Talley et al., 2005; Tsoflias et al., 2015)

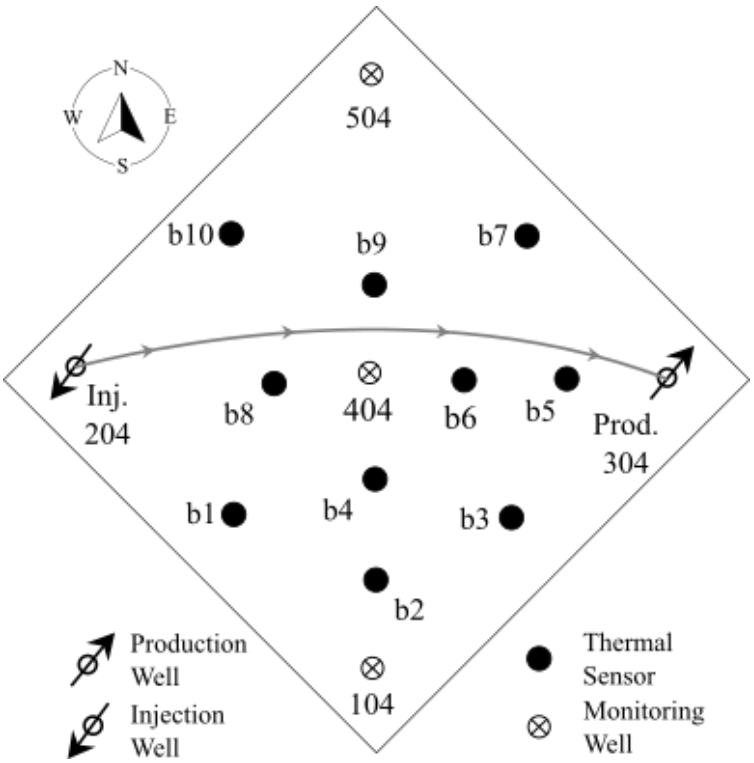

Figure 5: Five-spot well-field at the Altona Field Laboratory (AFL). Apart from the Ground Penetrating Radar (GPR) tracer imaging, all other experiments involved injection into well 204 and production from well 304. The "Thermal Sensor" markers represent the measurement locations for fracture/matrix heat exchange.

Three field tests at the AFL are particularly relevant to this study of surface area. These tests include: (1) an inert tracer test performed in 2012 in which hydraulic head was measured in the injection and production well (previously unpublished data); (2) a thermal test performed in 2015 in which heated fluids circulated through the relatively cold formation continuously for 6 days (Hawkins et al., 2017a); and (3) a combined inert/adsorbing tracer test performed in 2016 which estimated nominal interfacial surface area (Hawkins et al., 2018). Using tracer and hydraulic head measurements made in the 2012 inert tracer test, effective no-slip surface area is calculated by **Eq. (5)**.

4.1 Effective Area Calculation Result

Using the 2012 inert tracer test (**Fig. (6)**) data, the "modal" residence time τ_{modal} (Robinson et al., 1988) is assumed to correspond to the system's characteristic time, the interwell distance corresponds to the characteristic length, and the difference in interwell pressures at a specific flow rate is ΔP in **Eq. (5)**. The effective interwell volume then remains as the only unknown value. To estimate this value, the fraction of tracer mass recovered at the modal residence time multiplied by a factor of two χ is used to approximate the primary flow channel volume independent of the total system volume such that $V_{\mathrm{f}} = \chi Q \tau_{\mathrm{modal}}$. The doubled value is employed enable to distinguish a "fast" or "primary" flow channel from the total interwell fluid volume (Hawkins et al., 2017a).

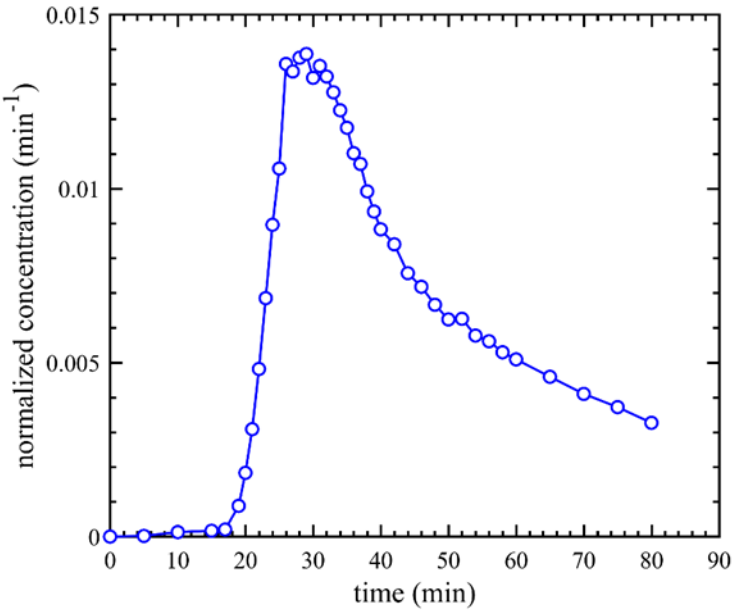

Figure 6: Measured passive tracer (iodine) breakthrough curve from the 2012 inert tracer test between injection well 204 and production well 304. The vertical axis is normalized by multiplying measured concentration (mg/L) by the ratio of volumetric flow rate (L/min) over iodide mass injected (mg).

In the 2012 passive tracer test, τ_{modal}, χ, and Q are 1740 s, 0.22, and 7x10^{-5} m^3/s, respectively. The resulting estimate of the primary flow path volume is $V_{\text{f}} = \chi Q \tau_{\text{modal}} = 2.68x10^{-2}$ m^3. Meanwhile, the measured frictional pressure drop was **433 Pa** (Solinst Levelogger® Model 2001) and the dynamic fluid viscosity is 1.0x10^{-3} Pa.s. Therefore, the effective surface area of the primary flow channel is **30.1** m^2.

Next, the 30.1 square meter estimate is compared to four independent estimates of surface area, including estimates that resulted from: 1.) an adsorbing tracer test; 2.) a thermal test; 3.) numerical modeling; and 4.) Ground Penetrating Radar (GPR) imaging of a saline tracer. Hawkins et al. (2017a) provides the area estimates via numerical modeling and the GPR tracer imaging. Hawkins et al. (2018) provides estimates of the primary flow channel interfacial area by the adsorbing tracer test. Finally, the analytical models provided in Robinson et al. (1988) and Murphy et al. (1981) provide the means to estimate surface area based on thermal drawdown.

Based on the numerical modeling, the primary flow channel width is roughly 0.9 m and the flow channel length is roughly 14.1 m, which results in an effective heat transfer area of roughly 25.4 m^2. Based on the GPR tracer imaging, the average flow channel width directly between the injector and producer is roughly 1.33 m and the flow channel length is roughly 14.1 m, which suggests a surface area of roughly 37.5 m^2. From the adsorbing tracer test surface area of the primary flow channel is roughly 28.3 m^2. Finally, based on the advection-conduction solutions, the surface area is roughly 27.2 m^2. Therefore, the novel estimate of 30.1 m^2 that is calculated here is in good agreement within the independent surface area estimates that have an average of 30 m^2 and a standard deviation of 5 m^2 (i.e., 30 ± 5 m^2.

5. CONCLUSIONS

The unique treatment of hydrodynamics presented resulted in **Eq. (4)**, which relates the frictional power loss of a fluid considering an arbitrary interfacial geometric shape. This treatment employs the Poiseuille number to quantify the unique impacts of specific geometric shapes, including internal flow through circular pipes ($N_{\text{Po}} = 2$) and parallel plates ($N_{\text{Po}} = 3$), and external flow around a sphere ($N_{\text{Po}} = 1/3$).

Eq. (4) provides a convenient means to calculate three-dimensional geometric properties from readily measured quantities such as pressure drop, tracer breakthrough curves, fluid density, and viscosity. **Eq. (5)**, for instance, is derived directly from **Eq. (4)** and enables one to estimate and effective area for "no-slip" laminar flow if joint pressure-tracer testing is performed. This estimate surface area is invaluable, because it can be employed in predictive forward models of fluid-solid interfacial phenomena such as advective heat transfer, adsorption, and molecular diffusion. In the context of geothermal reservoir engineering, the result of this work shows that premature thermal breakthrough resulting from short-circuited fluid flow in sparsely spaced discrete fractures can be anticipated before long-term circulation begins.

The challenge of constraining interfacial surface areas in subsurface reservoirs has been a well-established problem for more than fifty years. In this theoretical work, a simple analytical model is discovered that accurately estimates effective surface area given measurements of frictional pressure drop, modal residence time, and tracer mass fraction recovered. Using mesoscale field measurements, the theoretical

development is then validated by estimating a surface area of **30.1** m^2. This estimate is in good agreement with four independent estimates that result in a value of $\mathbf{30 \pm 5\ m^2}$.

REFERENCES

Bahrami, M., Yovanovich, M.M., and Culham, J.R.: Pressure drop of fully-developed, laminar flow in microchannels of arbitrary cross-section, Journal of Fluids Engineering, 128, (2006), 1036.

Batchelor, G.K.: *An Introduction to Fluid Dynamics* (Cambridge University Press, 2000).

Cassidy, M., Manga, M., Cashman, K., and Bachmann, O.: Controls on explosive-effusive volcanic eruption styles, Nature Communications, 9, (2018).

Gloss, D., and Herwig, H.: Wall roughness effects in laminar flows: an often ignored though significant issue, Experiments in Fluids, (2010), DOI 10.1007/s00348-009-0811-6.

Guiltinan, E., and Becker, M.W.: Measuring well hydraulic connectivity in fractured bedrock using periodic slug tests, Journal of Hydrology, 521, (2015), 100-107.

Hawkins, A.J., Fox, D.B., Becker, M.W., and Tester, J.W.: Measurement and simulation of heat exchange in fractured bedrock using inert and thermally degrading tracers, Water Resources Research, 53, (2017a), 1210-1230.

Hawkins, A.J., Becker, M.W., and Tsoflias, G.P.: Evaluation of inert tracers in a bedrock fracture using ground penetrating radar and thermal sensors, Geothermics, 67, (2017b), 86-94.

Hawkins, A.J., Becker, M.W., and Tester, J.W.: Tester, Inert and adsorptive tracer tests for field measurement of flow-wetted surface area, Water Resources Research, 54, (2018), 5341-5358.

Hawkins, A.J., Fox, D.B., Koch, D.L., Becker, M.W., and Tester, J.W.: Predictive inverse model for advective heat transfer in a short-circuited fracture: Dimensional analysis, machine learning, and field demonstration, Water Resources Research, 56, (2020), e2020WR027065.

Janasek, D., Franzke, J., and Manz, A.: Scaling and the design of miniaturized chemical-analysis systems, Nature, 442, (2006), 374-380.

Lee, S.J., Kang, D., Lee, S.C., and Ha, Y.-R.: Peculiar liquid-feeding and pathogen transmission behavior of *Aedes togoi* and comparison with *Anopheles sinensis*, Scientific Reports, (2016), 6.

Murphy, H.D., Tester, J.W., Grigsby, C.O, and Potter, R.M.: Energy extraction from fractured geothermal reservoirs in low-permeability crystalline rock, Journal of Geophysical Research, 86, (1981), 7145-7158.

Mutch, E.J.F., Maclennan, J., Shorttle, O., Edmonds, J.F.: Rudge, Rapid transcrustal magma movement under Iceland, Nature Geoscience., 12, (2019), 569.

Oh, K.W., Lee, K., Ahn, B., and Furlani, E.P.: Design of pressure-driven microfluidic networks using electric circuit analogy, Lab on a Chip, 12, (2012), 515.

Robinson, B.A., Tester, J.W., and Brown, L.F.: Reservoir sizing using inert and chemically reacting tracers, SPE Formation Evaluation, (1988), 227-234.

Secchi, et al.: Massive radius-dependent flow slippage in carbon nanotubes, Nature, 537, (2016), 210.

Stone, H.A., Stroock, A.D., and Ajdari, A.: Engineering flows in small devices: Microfluidics toward a lab-on-a-chip, Annual Reviews of Fluid Mechanics, 36, (2004), 381.

Talley, J., Baker, G.S., Becker, M.W., and Beyrle, N.: Four dimensional mapping of tracer channelization in subhorizontal bedrock fractures using surface ground penetrating radar, Geophysical Research Letters, 32, (2005), L04401.

Tester, J.W., Beckers, K.F., Hawkins, A.J., and Lukawski, M.Z.: The evolving role of geothermal energy for decarbonizing the United States, Energy and Environmental Science, 14, (2021), 6211.

Tsoflias, G.P., Perll, C., Baker, M., and Becker, M.W.: Cross-polarized GPR imaging of fracture flow channeling, Journal of Earth Science, 26, (2015), 776-784.

Zouache, M.A., Eames, I., Klettner, C.A., Luthert, P.J.: Form, shape and function: segmented blood flow in the choriocapillaris, Scientific Reports, ***6***, (2016), 1.